

Characterisation of the **surface geometry** of 3D printed scaffolds for cell infiltration and surgical suturing

Laura Ruiz-Cantu^{1*}, Andrew Gleadall^{2*}, Callum Faris³, Joel Segal², Kevin Shakesheff¹ and Jing Yang¹

*Laura Ruiz-Cantu and Andrew Gleadall had equal contributions.

1. Drug Delivery and Tissue Engineering, Faculty of Science, University of Nottingham, University Park, Nottingham, NG7 2RD, UK

2. Manufacturing and Process Technologies, Faculty of Engineering, University of Nottingham, University Park, Nottingham, NG7 2RD, UK

3. Nottingham University Hospital, Department of Otorhinolaryngology, Derby Road, Nottingham, NG7 2UK, UK

Abstract

3D printing is of great interest for tissue engineering scaffolds due to the ability to form complex geometries and control internal structures, including porosity and pore size. The porous structure of scaffolds plays an important role in cell ingrowth and nutrition infusion. Although the internal porosity and pore size of 3D printed scaffolds have been frequently studied, the surface porosity and pore size, which are critical for cell infiltration and mass transport, have not been investigated. The **surface geometry** can differ considerably from the internal scaffold structure depending on the 3D printing process. It is vital to be able to control the **surface geometry** of scaffolds as well as the internal structure to fabricate optimal architectures. This work presents a method to control the surface porosity and pore size of 3D printed scaffolds. Six scaffold designs have been printed with surface porosities ranging from 3% - 21%. We have characterised the overall scaffold porosity and surface porosity using optical microscopy and microCT. It has been found that surface porosity has a significant impact on cell infiltration and proliferation. In addition, the porosity of the surface has been found to have an effect on mechanical properties and on the forces required to penetrate the scaffold with a surgical suturing needle. To the authors' knowledge, this study is the first to investigate the **surface geometry** of extrusion-based 3D printed scaffolds and demonstrates the importance of **surface geometry** in cell infiltration and clinical manipulation.

1. Introduction

The use of 3D printing in tissue engineering and regenerative medicine has been spreading rapidly in recent years. The combination of this technology and medical imaging enables the creation of patient-specific implants and the reproduction of the complex architecture of tissues [1, 2]. Tissue engineering constructs and implants have been 3D printed for a range of applications including heart valves [3], ears [4], articular surface [5], meniscus [6], trachea splint [7], bone [8], cranium [9], mandible [10] and distal femur [11].

Several 3D printing techniques have been used for tissue engineering applications including fused deposition modelling (FDM), stereolithography, inkjet printing, selective laser sintering and laser assisted bioprinting [12]. FDM is a process in which the material is melted and extruded in filaments layer-by-layer to form a 3D structure [13]. Advantages of this technique are that it contains no toxic solvents, has no waste of material and is low cost [14]. However, a major disadvantage is the pore occlusion at the surface due to the build-up of the materials at the surface during the printing process [15]. Many studies have investigated FDM but have focused on characterising the internal porosity and architecture of the printed structures [16, 17]. Very little attention has been paid to surface porosity.

The pore size and porosity at the surface play an important role in cell ingrowth and vascularisation [18, 19]. Previous studies have reported the need of pores at least 100 μm in diameter for successful exchange of nutrients and oxygen for cell survival [20]. Pores between 400 and 600 μm have been shown to increase bone formation [21]. In addition to this, the surface porosity may also affect surgical suturing through scaffolds. Implants are usually required to be secured in situ to prevent migration and extrusion. Suturing through scaffolds is an efficient way of securing the implant position in the host tissues. In addition to securing the implant, sutures can be used to secure free cartilaginous, osseous or vascularised osseous free flaps to the framework scaffold. This lamination of the framework scaffold with autologous grafts (free and vascularised) creates a composite graft/implant that can then be inserted into the recipient tissue bed. In these instances the scaffold acts as a surgical guide, aiding the surgeon in reconstruction of highly complex 3D structures, such as in total nasal reconstruction.

An important factor in suturing is the force required to penetrate the needle through the material being sutured. Several studies have investigated the effect of needle geometry on the penetration force [22-24]. In addition, it has been suggested that forces generated during insertion of a suturing needle may result in a loss of chondrocytes near the needle [25]. To our knowledge, no studies have investigated the needle penetration forces in 3D printed scaffolds.

For the reasons mentioned above, it is important to be able to control the surface porosity and pore size of 3D printed scaffolds. These surface properties depend greatly on the print head path in each layer during the printing process. Current commercial 3D printing software programs that decide the print head path have not considered the effect of the printing path on the surface architecture of scaffolds. Therefore, we have developed a software program to control the printing path. This study represents a part of our strategy on total nasal reconstruction using 3D printed constructs. The focus of this study is to investigate the surface geometry of 3D printed scaffolds. Scaffolds are 3D printed with varying surface porosities and pore sizes in order to understand the effect of the surface on cell infiltration and suturing.

2. Materials and methods

2.1. Scaffold design and fabrication

Figure 1 shows 3D representations of the six scaffold structures utilised in this study. They were designed to give a range of surface porosities using newly-developed software integrated into an Excel spreadsheet ("Scaffold Designer" in supplementary). It generates machine-code that is imported into the *3D Discovery HMI* software supplied with the *REGENHU 3D Discovery* bioprinter. The scaffolds were designed with overall dimensions $16.8 \times 2.4 \times 4.8 \text{ mm}^3$ (length x width x height). The term *surface porosity* is used to refer to the porosity of the *side-walls* of the 3D printed scaffolds as highlighted by the dashed box in the figure. The figure shows how different surface porosities and pore sizes were achieved by controlling two design-aspects of the 3D printed scaffolds: the *end angle* and the number of *repeated layers*. The *end angle* refers to the angle at which the printhead moves from the end of one printed strand to the beginning of the next parallel strand. It was set to be either 45° or 90° . The number of *repeated layers* refers to the number of consecutive layers with the same printing path.

Scaffolds were 3D printed on a REGENHU 3D Discovery bioprinter in a custom-built enclosure with an air temperature of 27°C and 35% relative humidity. Polycaprolactone (PCL) pellets ($M_n = 40,000 - 50,000 \text{ g mol}^{-1}$ Sigma-Aldrich, UK) were extruded at a temperature of 77°C . PCL was

chosen because it has been used in cartilage tissue engineering [26, 27]. It is biocompatible, FDA approved, and has a degradation time longer than the period of scar tissue formation and maturation (ca. 12 months) after nasal reconstruction, and the contractile force exerted by scar tissue could deform the reconstructed nose shape [28].

The printhead travelled at a rate of 16 mm s^{-1} and the pressure of the PCL melt chamber was 2 bar. In order to maintain a constant internal scaffold structure, the following printing parameters were kept constant for all scaffold designs: the distance between the centres of parallel printed strands was set to $600 \mu\text{m}$; the bioprinter extruder feed rate **program parameter** was set to **20 revolutions per metre of printhead travel**, which produced a strand diameter of $307 \mu\text{m}$; and the height increase of the printhead between layers was set to $175 \mu\text{m}$. A layer fan (Nanoxia Deep Silence), running at 800 rpm (14.4 - 15.8 cfm), was aimed at the scaffolds at a distance of 200 mm to ensure layers were cooled to a suitable degree to support subsequent printed layers.

Three identical scaffolds were printed on each run. For mechanical compression testing, microCT scanning and biological characterisation, three samples of size $3.6 \times 2.4 \times 4.8 \text{ mm}^3$ (length x width x height) were cut from each printed scaffold using a scalpel. Surface characterisation, cell seeding and needle penetration tests were conducted through the 3D printed *side-wall* as opposed to the newly cut surface.

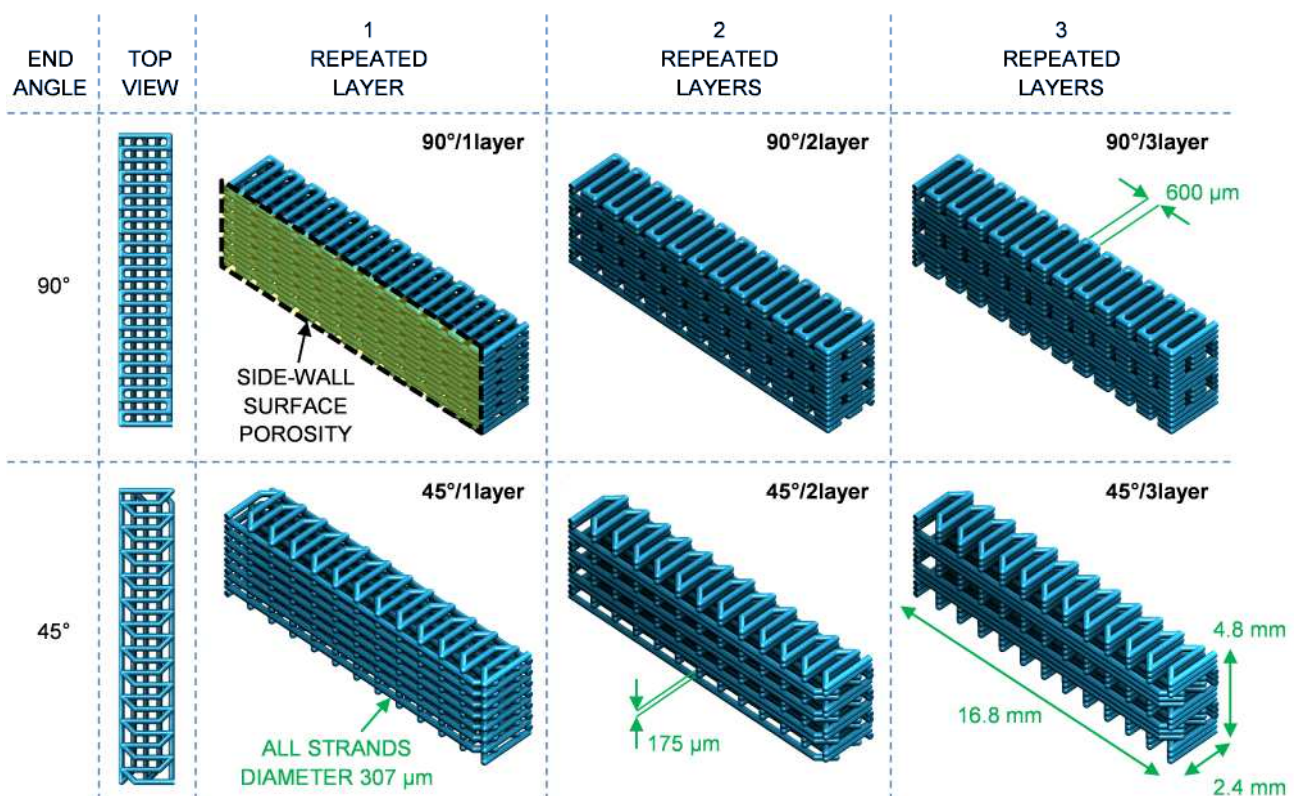


Figure 1. Schematic of the six scaffold types investigated in this study. The angle at which the printhead moves from the end of one strand to the beginning of a parallel strand (the *end angle*) is set to either 90° or 45° in order to control surface porosity. Also, identical layers are printed 1, 2 or 3 times before changing to a perpendicular orientation.

2.2. Microscopy

Microscopy was performed using a Zeiss Stemi 2000-C microscope with a Schott S40-10D ring light to assess surface porosity and pore size. Greyscale images with a pixel size of $2.8 \mu\text{m}$ were

binarised according to greyscale value (0 - 255) using thresholds of 185 - 235. A range of thresholds was necessary due to greater illumination towards the centre of samples.

2.3. Micro Computed Tomography (microCT)

Samples were analysed using Skyscan 1172 (Skyscan, Belgium) desktop X-ray CT scanner with a pixel resolution of 6.7 μm , X-ray source current 800 μA and voltage 50 kV. Samples were mounted vertically and rotated thorough 360°. Images were recorded every 0.400° of rotation. These images were reconstructed using the NRecon software (Skyscan, Belgium). Porosity was quantified with 3D histomorphometric analysis using the CTAn software by thresholding the sample lower grey 27 upper grey 85. The 3D models were created using the same software with a pixel resolution of 17.2 μm .

The surface of the 3D models was isolated using the netfabb Basic software (netfabb, Germany) to quantify porosity and pore size. Binary images of the surfaces were used for porosity characterisation using the ImageJ software.

For the reconstruction of the cell-seeded samples, cells were stained with osmium tetroxide and the previous method was used to isolate the cells from the 3D pictures. The thresholds for the cells were lower grey 106 and upper grey 255.

2.4. Mechanical compression testing

Compressive tests were conducted following ASTM standard D695. An Instron 5969 machine with a 5 kN load cell was used to compress unconstrained samples between two steel plates at a rate of 1 mm min⁻¹ to 33% strain. Three samples were tested for each scaffold design. They were compressed parallel to the build-direction (the direction in which layers were built-up during 3D printing process). The compressive moduli were calculated for all samples using a linear-elastic compression phase as the applied force increased from 10 to 50 N.

2.5. Cell isolation and seeding

Cartilage tissue was harvested from the condyle of two sheep. Chondrocytes were isolated through an enzymatic digestion with 0.2% collagenase type II (Sigma-Aldrich, UK) for 4 hours at 37°C. The cell suspension was passed through a 70 μm nylon strainer (Fisher, UK) and centrifuged at 700 x g for 5 minutes. Cells were plated and cultured with α -MEM supplemented with 10% (v/v) foetal calf serum (FCS), 1% MEM non-essential amino acids solution (Sigma-Aldrich, UK), 1% antibiotic/antimicotic (Sigma-Aldrich, UK), 1% L-glutamine (Sigma-Aldrich, UK) and 0.025 g/ml of ascorbic acid (Sigma-Aldrich, UK). Passage 3 chondrocytes were detached using trypsin EDTA (Sigma-Aldrich, UK); counted and centrifuged at 700 x g for 5 min. Cells were resuspended according to experiment concentrations needed.

The PCL 3D printed samples were disinfected with 70% industrial methylated spirit (IMS) for 24 hours, washed 5 times with phosphate buffer saline (PBS) and incubated overnight with FCS containing 2% antibiotic/antimitotic for protein adsorption. The samples were fully saturated with FCS before being transferred into the seeding vessels.

For static seeding, the 3D printed scaffolds pre-saturated with FCS were placed into 96-well plates leaving one of the *side-walls* (Figure 1) facing upwards. We followed a static seeding method used previously elsewhere [29]. A suspension of 800,000 cells in 50 μl was pipetted on the top of one of the *side-walls* of the scaffolds. Cells were left to attach for 2 hours and subsequently samples were transferred to a new well containing 200 μl of medium. Medium was changed every three days. Twenty samples of each condition were seeded.

For dynamic seeding, the 3D printed scaffolds were placed inside KIYATEC 3DKUBE™ (KIYATEC, USA) chambers with one of the *side-walls* facing the inlet of the chamber the other *side-wall* facing the outlet. A 3 ml cell suspension containing 800,000 cells was inoculated into the silicon tubing (Altec, UK) connected to the KIYATEC 3DKUBE™. The cell suspension was perfused in a closed-loop for individual samples using a peristaltic pump (Watson Marlow 323, UK) at a flow rate of 0.5 ml min⁻¹ for 1 hour. Perfusion was stopped and cells were left to attach to the scaffolds for 2 hours. Four samples of each condition were seeded. Three were used for DNA quantification assay and one for osmium tetroxide staining.

2.6. Cell number quantification and proliferation

Cell number was evaluated by DNA quantification using Quant-iT™ PicoGreen® dsDNA Assay Kit (Life technologies, USA). Samples were freeze thawed three times for membrane disruption. Cells were lysed according to the manufacturer protocol. The fluorescence intensity was measured to quantify the amount of DNA using a TECAN plate reader (Tecan, Switzerland) at an excitation of 480 nm and emission of 560 nm. The number of cells was correlated with the fluorescence intensity using a calibration curve.

Cell proliferation was determined on days 1, 7 and 14 using a cell viability reagent PrestoBlue® (life technologies, USA). Samples were incubated for 1.5 hours in the PrestoBlue® solution. Fluorescence intensity was measured at an excitation of 520 nm and emission of 590 nm.

2.7. Osmium tetroxide and histological staining

Samples were fixed using 3% glutaraldehyde (Sigma-Aldrich, UK). Fixation was performed overnight at 4°C. After fixation, samples were washed with PBS and stained with 1% osmium tetroxide for 2 hours. Samples were then washed and left to dry in a fume hood for 4 days before microCT scanning.

For the histological staining, the samples were fixed with 7% paraformaldehyde for 2 hours at 4°C. After fixing, samples were washed with PBS and stained using toluidine blue for 2 hours followed by washing. Samples were then sectioned and imaged under a microscope (Nikon SMZ1500, UK).

2.8. Needle penetration testing

Needle penetration tests were conducted following ASTM standard F3014 on an Instron 5969 machine using a straight surgical needle (Ethicon SC-1 nasal septal needle) moving at a rate of 100 mm min⁻¹ with a 5 kN load cell. The needle was chosen because it is used in rhinoplasty and otoplasty procedures [30-33]. The diameter was measured as 430 µm. The scaffolds were oriented perpendicular to the build-direction so that the needle penetrated one *side-wall*, as highlighted in **Figure 1**, on entry to the scaffold and penetrated the opposite *side-wall* to exit the scaffold. They were placed unconstrained on a steel plate above a 2 mm diameter hole to allow the needle tip to exit the lower surface of the scaffold by a distance of 6 mm. Twenty needle penetration tests were completed for each scaffold design at random positions. A new needle was used for each scaffold design. The maximum needle penetration force was calculated for each scaffold design as the average maximum force of all 20 tests for that scaffold. Average plots for needle penetration force versus distance were calculated by averaging the 20 individual test plots.

2.9. Statistical analysis

Statistical analysis was performed using Prism version 6.0 (GraphPad Software, USA). Statistical significance was determined by two-way ANOVA followed by uncorrected Fisher's Least Square Difference multiple-comparison post hoc test. Plots are mean with error bars indicating SEM.

3. Results and discussion

3.1. Porosity and pore size characterisation

The six structures with one, two or three *repeated layers* and *end angles* of 45° and 90° were analysed using microCT and optical microscopy. The *end angle* affects the print path near the surface of the scaffolds and the number of *repeated layers* affects the order in which printed strands are laid down on top of one another. Both parameters can be used to control the size and shape of pores.

Figure 2 shows microscope and microCT images of the six different scaffolds. **Figures 2a** and **2b** show top-views of the 90° and 45° *end angle* scaffolds; **Figure 2c - 2h** show the 3D printed *side-walls*. It can be seen from **Figure 2a** that there is a build-up of polymer at the *side-wall* of the scaffold when the printhead changes direction because there are only three pores in the top row of pores in the figure, adjacent to the *side-wall*, compared to five pores in the middle two rows in the figure. Surface porosities for the *side-wall* of the six scaffold designs are plotted in **Figure 3a**. On average for all samples, the 45° *end angle* scaffolds demonstrated 348% greater surface porosity than the 90° *end angle* scaffolds with equivalent *repeated layers*. This is because the pores were wider, as can be clearly seen in **Figures 2g** and **2h**. A similar trend can also be seen when comparing **Figure 2c** to **2d** and **2e** to **2f**. The two top-view images, **Figures 2a** and **2b**, indicate that the 45° *end angle* samples have wider pores because less polymer is 3D printed at or near the *side-wall* as highlighted by the triangular region.

Figure 3b shows the pore sizes measured for the different scaffold designs. On average for all scaffolds, the 45° *end angle* samples had 361% larger pore sizes than 90° samples with equivalent *repeated layers* since the pores are wider, as discussed above. In addition, increasing the number of *repeated layers* increased the height of pores and therefore pore size, as can be seen in **Figure 2**. The 3 *repeated layer* samples had an average pore size 434% larger than the 1 *repeated layer* samples with equivalent *end angles*.

The bulk porosities of samples measured by microCT are shown in **Figure 3c**. There was a slight increase in porosity of the 45° *end angle* samples because the printhead travelled along a shorter print-path for each layer (due to cutting corners) and therefore deposited less polymer. However, on average for all scaffolds, the 45° *end angle* samples demonstrated just 12.7% increase in bulk porosity versus 90° samples with equivalent *repeated layers*. This is over an order of magnitude less than the effects of *end angle* on surface pore size and surface porosity. And increasing the number of *repeated layers* from one to two or three had less than 8.5% effect on bulk porosity. Therefore, the *end angle* and *repeated layer* design variables are able to control surface porosity and surface pore size with little impact on bulk porosity.

Surface porosity and pore size measurements were also calculated through microscopy. And bulk porosities were also calculated based on the relative density of the printed scaffolds versus solid PCL. All three results displayed similar trends to microCT measurements and are provided in supplementary **Figure S1**. As shown in **Figure 3** and **Figure S1**, optical microscopy and microCT can both be used to measure pore size. The choice of imaging technique depends on the pore size to be measured and the required imaging resolution. MicroCT offers the benefit of being able to easily isolate the surface pores due to the higher contrast of images.

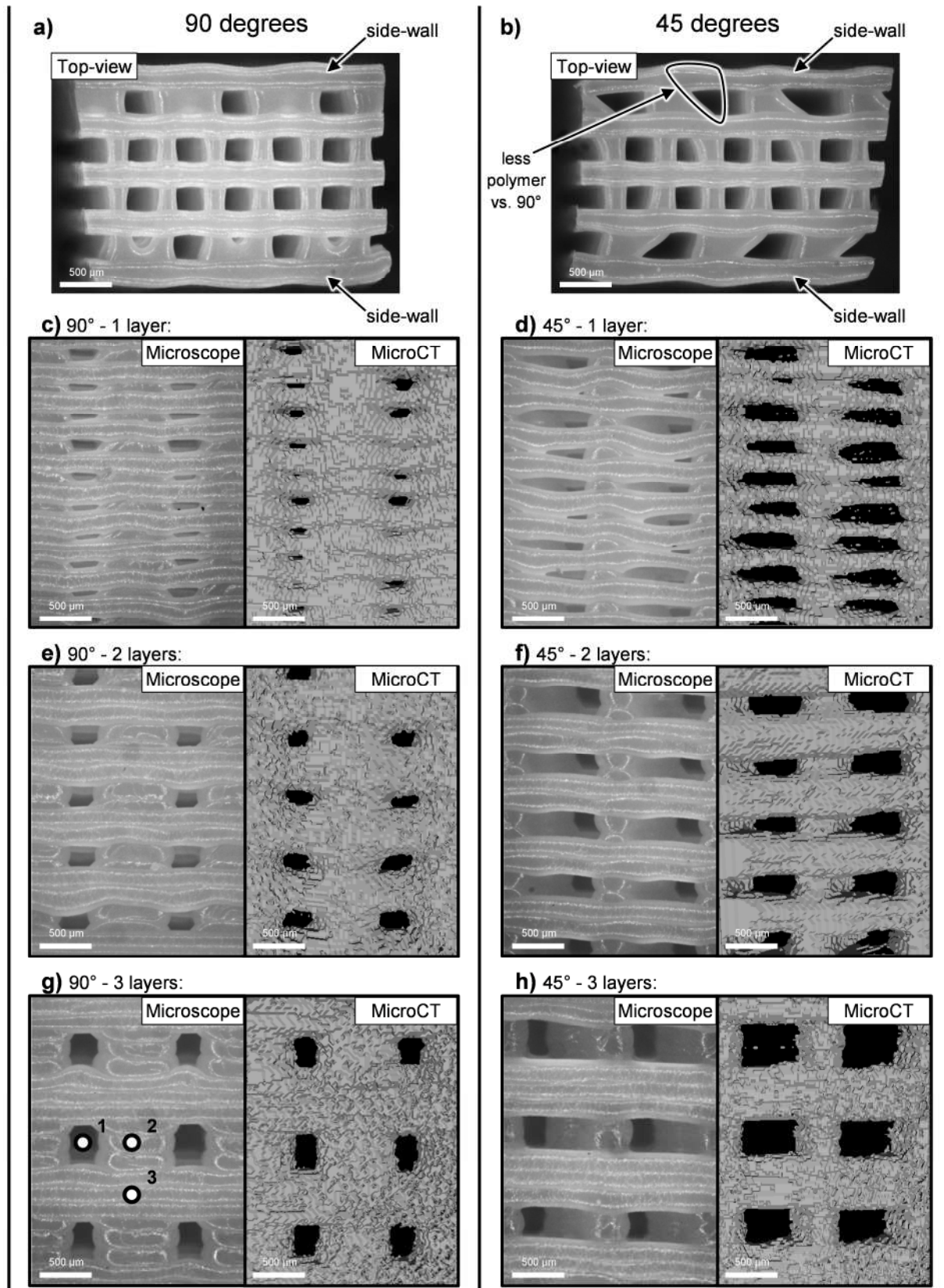


Figure 2. Microscope and microCT images of the different scaffold designs. (a) and (b) are top view microscope images. (c), (e), & (g) are microscope and microCT images for the 90° *end angle* samples with 1, 2 & 3 *repeated layers* respectively. (d), (f) & (h) are images for the 45° *end angle* samples with 1, 2 & 3 *repeated layers* respectively. Points 1, 2 & 3 in (g) are discussed in relation to **Figure 10**.

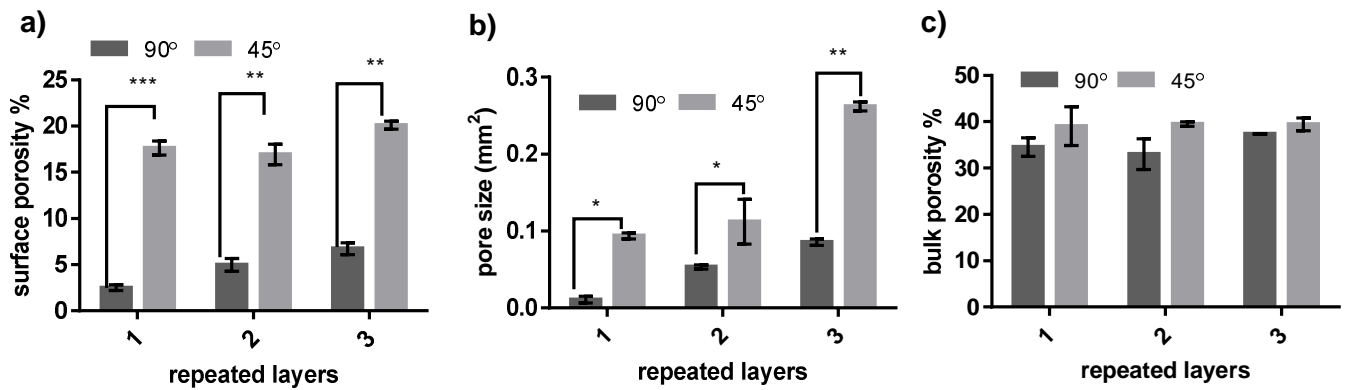


Figure 3. (a) Surface porosity measured from microCT images, (b) average pore size, and (c) bulk porosity calculated for the different scaffold designs based on microCT images. * $p < 0.05$, ** $p < 0.009$

3.2. Mechanical characterisation

The compressive moduli measured for each scaffold design are presented in **Figure 4a** and a typical force-displacement curve is shown in **Figure 4b**. The 45° *end angle* samples demonstrated an average reduction in compressive modulus of 21.3% versus the 90° samples. This reduction is likely due in part to the reduction of bulk porosity. Furthermore, **Figure 2** shows that the 90° samples have almost solid *side-walls*. Solid walls can considerably affect mechanical properties as demonstrated by Eshraghi and Das [34] who found scaffolds with solid walls to have a compressive modulus of 133.4 MPa versus 12.1 MPa for those without, whilst porosity only reduced from 61.9% to 44.8%. For larger scaffolds, the *side-walls* may have less of an effect on overall scaffold stiffness because the majority of the mechanical properties will be dictated by the large internal region of the scaffolds. However, the geometry of a scaffold may require a thin wall to suit a particular clinical application, such as a scaffold for nasal reconstruction (supplementary **Figure S2**), in which case the 3D printed *side-wall* is an important factor that must be considered with regards to stiffness.

The effect of *end-angle* on surface porosity and pore size (**Figure 3a** and **Figure 3b**) was over an order of magnitude greater than the effect on compressive modulus. Similarly, increasing the number of *repeated layers* from one to two or three affected surface pore size by up to 434% but had less than 9% effect on modulus. Other design factors including the strand width and spacing between strands have been shown to have a much larger effect on modulus [35]. Therefore, the *end-angle* and number of *repeated layers* may be used to control the surface properties whilst alternative design aspects predominantly dictate mechanical properties, internal porosity and internal pore size.

The samples in this study had relatively low bulk porosities (25-36%). Consequently their moduli were within the cancellous bone range and higher than those reported for cartilage. Human cartilage has been found to have a compressive modulus in the range of 0.44 to 20.4 MPa [36-38]. Increasing porosity has been shown to be able to decrease modulus. 3D printed PCL scaffolds showed compressive moduli ranging from 4 to 77 MPa with porosities between 48% and 77% [39]. Regardless of design on mechanical properties, the printing method presented in this study can be implemented to control surface pore dimension which is shown to be important for cell infiltration, nutrient exchange and suturing as discussed later.

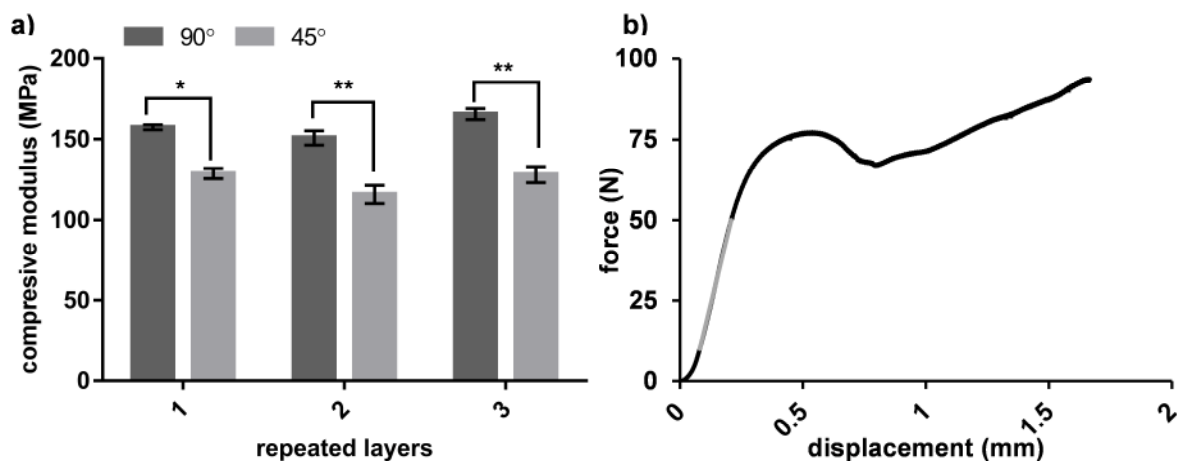


Figure 4. (a) Compressive moduli for the six scaffold designs. (b) A force-displacement plot for a 90°/3layer sample. The grey line indicates the 10 - 50 N region used to calculate compressive modulus. * $p < 0.05$ ** $p < 0.009$

3.3. Cell infiltration and proliferation

3.3.1 Cell infiltration

In order to investigate the effect of surface porosity and pore size on cell infiltration into the scaffolds, we seeded cells using a static method and a dynamic method. Chondrocytes were used as a model cell type. More cells were found in the scaffolds with the static method compared to the dynamic method, as shown in **Figure 5a** and **5c**. As the same number of cells was used in both seeding methods, the difference in cell number within the scaffolds was likely due to the loss of cells in the tubing in the dynamic method.

As shown in **Figure 5a**, for samples with 1 and 2 *repeated layers* seeded using the static method there is no significant difference in cell number between the different *end angles*. However for samples with 3 *repeated layers*, a 90° *end angle* resulted in 70% more cells in the scaffold after static seeding compared to 45° *end angle*. This may be due to **pores larger than 0.1 mm² in cross section having** allowed the cell suspension to freely pass through the scaffold during seeding. In the static method the cell suspension enters the scaffold by gravity. **Although all the suspension enters the scaffold,** the amount that leaves the scaffold depends on the surface pore size and porosity; more liquid could pass through and leave the scaffold with high porosity and pore size. There is no correlation between cell number and pore size ($R^2 = 0.39$, **Figure 5a**) or porosity ($R^2 = 0.15$, **Figure 5a**).

With the dynamic method, the number of cells seeded was on average 1.4 times higher in 45° *end angle* samples compared to 90° *end angle* samples for all *repeated layers* (**Figure 5b**). There is no correlation between pores size and cell number ($R^2 = 0.076$) whereas there is a weak correlation ($R^2 = 0.62$) between porosity and cell number (**Figure 5b**). Similar results were reported in a previous study that showed increased seeding efficacy with increased permeability of the scaffold when the cells were seeded using a perfusion system that is similar to the one we used in this study [40]. The permeability of a scaffold depends on porosity, pore size and pore orientation; when porosity and pore size are increased the permeability is increased as well [41]. If the permeability is low the liquid is **more likely to travel** around rather than through the scaffold and consequently fewer cells enter the scaffold.

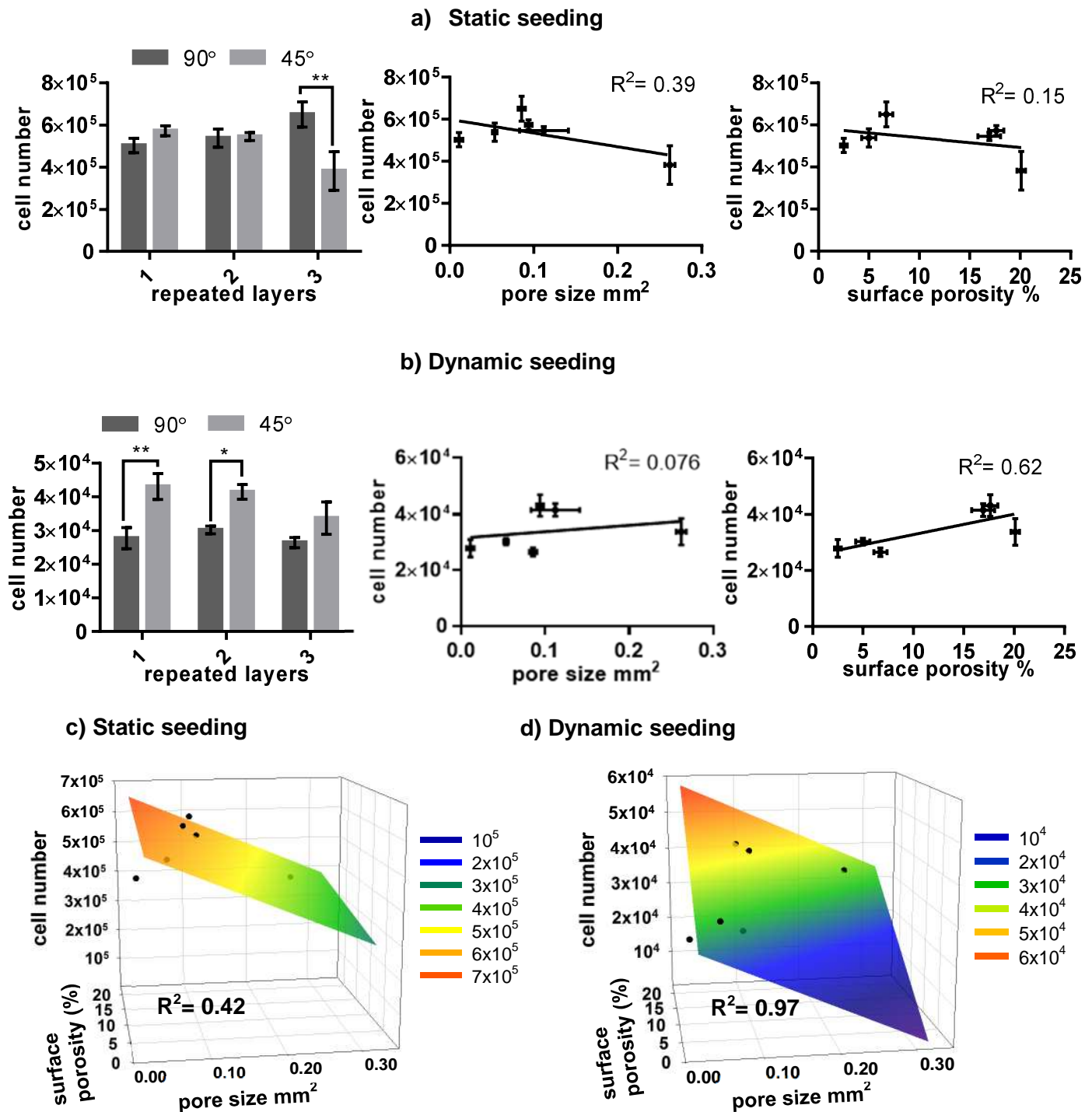


Figure 5 Cell infiltration into 3D printed scaffolds using both static and dynamic seeding methods. (a) and (b) Cell number with static and dynamic seeding, individual relation between pore size, porosity and cell number. (c) and (d) 3D plots representing the relation between pore size, porosity and cell number with static and dynamic seeding. Colour plane represents the multivariate (pore size and porosity) correlation based on the six measured data points. * p < 0.05, ** p < 0.009.

To investigate the combined effect of porosity and pore size, we have plotted cell number versus these two parameters (**Figure 5c** and **5d**). Multivariate regression analysis (colour planes) was performed for both seeding methods. Interestingly, a strong correlation (R²=0.97) was identified for the dynamic method whereas the correlation for the static method is still weak (R²=0.42). This

finding suggests that cell infiltration is linearly dependent on both the pore size and porosity for dynamic seeding, whereas a simple relationship does not exist for static seeding.

We also investigated the distribution of seeded cells in the scaffolds. As shown in **Figure 6** cells tended to form aggregates predominantly at the intersections of the strands. This pattern has been previously observed with osteoprogenitor cells growing on PCL scaffolds manufactured by fused deposition modelling [42]. The cell aggregation at strand intersections could be due to the meniscus formation of cell suspension at these locations, which enhanced the retention of cells. To closely examine the cells within the structure we sectioned the samples and stained the cells with toluidine blue. **Figure 7** shows blue-stained cell colonies growing at intersections.

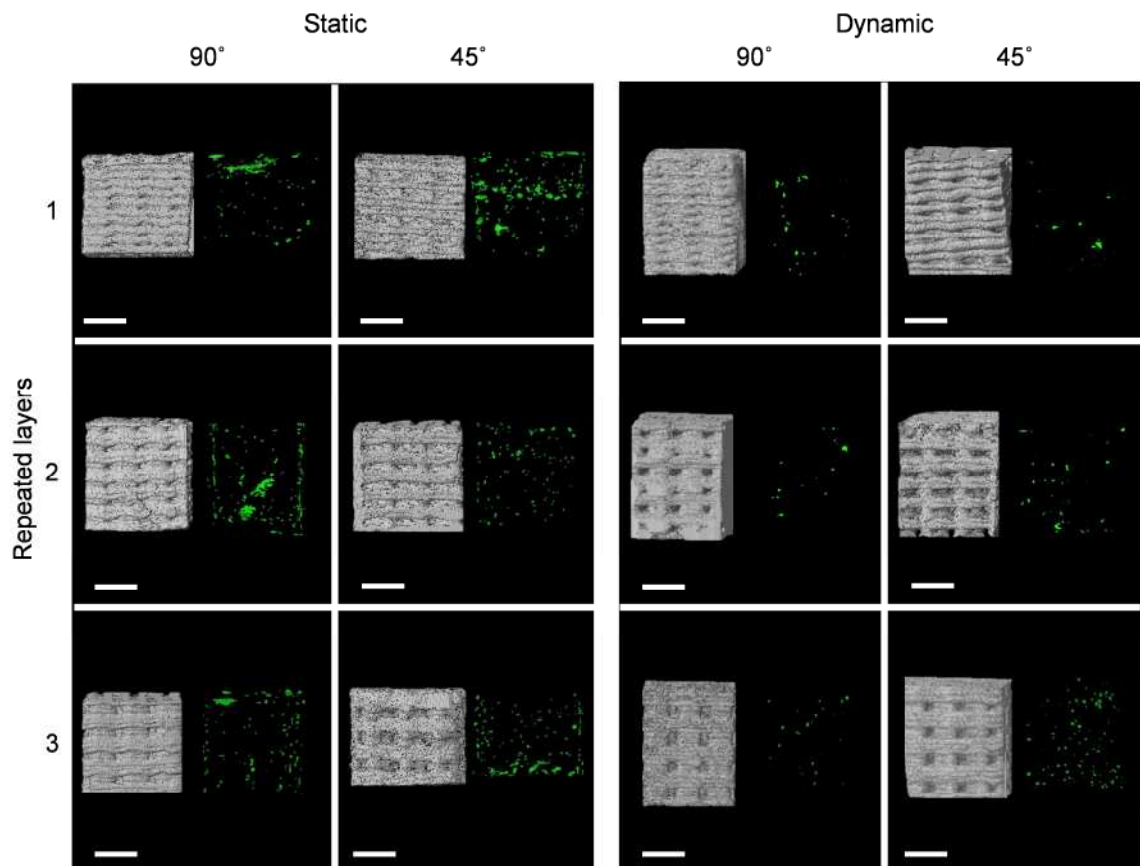


Figure 6. Cell distribution inside the scaffolds on day 1 for static and dynamic seeding. Both scaffolds and cells were imaged using microCT, the cells were false coloured. Scale bars represent 1 mm.

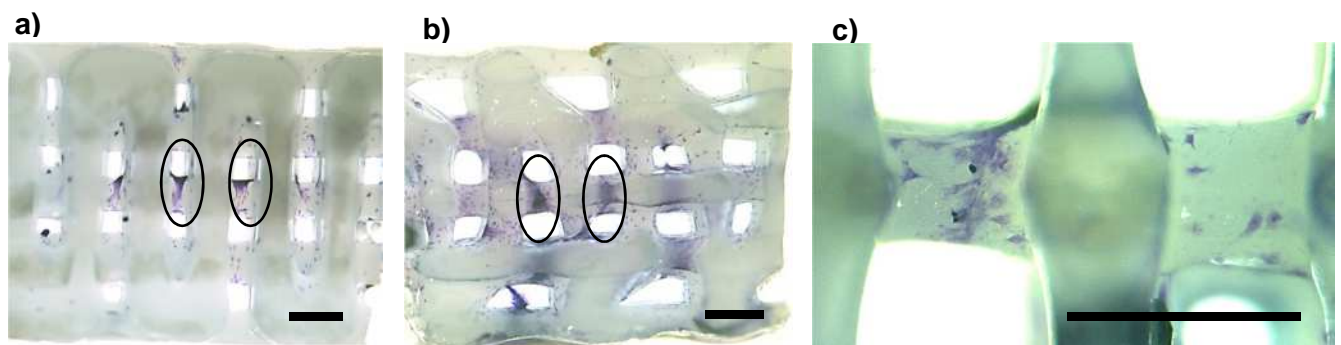


Figure 7. Representative images of chondrocytes stained with toluidine blue after 4 days in culture showing cell attachment and distribution. (a) Chondrocytes distribution in 90° *end angle* scaffold. (b) Chondrocytes distribution in 45° *end angle*. (c) Closer view of cells attached to PCL strands. Scale bars represent 0.5 mm.

3.3.2 Cell proliferation

The surface porosity and pore size also have an effect on nutrients and waste exchange, which affects cells viability and proliferation [43]. Therefore, we cultured the cell-seeded scaffolds to investigate how surface permeability affects the proliferation of the cells in static culture conditions. Samples with one *repeated layer* showed an increase in metabolic activity for both of the *end angles* but 45° had a statistically significant higher increase on day 7 and 14 (**Figure 8a**). The same trend was observed on the samples with two *repeated layers* (**Figure 8b**). For the three *repeated layers* samples there was no difference observed at day 7 but a statistically significant higher increase was noticed for 45° samples on day 14 (**Figure 8c**). The higher surface porosity and pore size associated with the three layers scaffolds might cause better mass exchange up to 7 days. The lower proliferation rate in scaffolds with 90° end angles could be due to the lower surface permeability and consequently lower exchange rate of nutrients and waste, which has been reported previously [44].

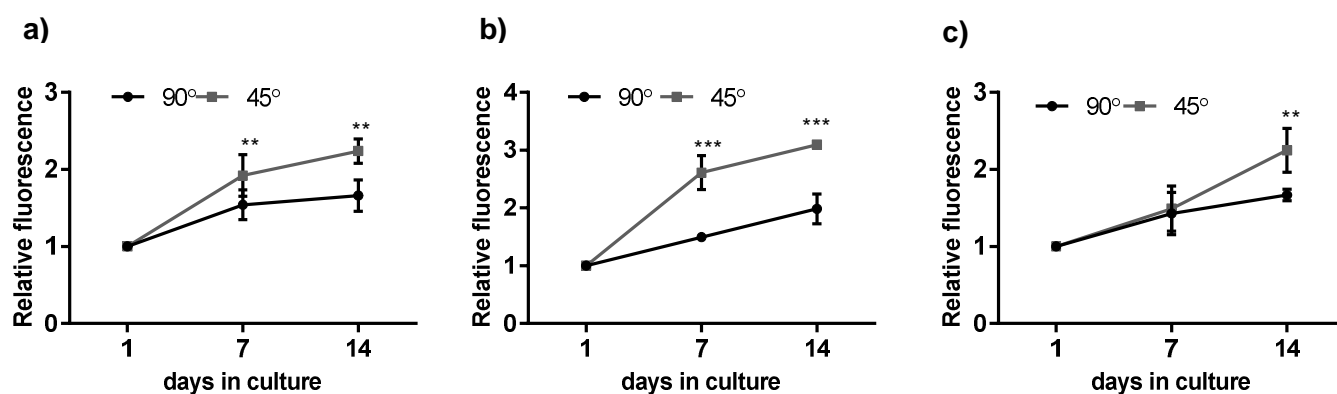


Figure 8. Cell metabolic activity of static seeded samples after 7 and 14 days in culture. (a) One *repeated layer* scaffolds, (b) two *repeated layer* scaffolds, (c) three *repeated layer* scaffolds. * $p < 0.05$, ** $p < 0.009$, *** $p < 0.0009$.

3.4. Needle penetration testing

Needle penetration tests were conducted to identify the effect of the 3D-printed *side-wall* on the forces required for penetration during surgical suturing. **Figure 9a** shows the maximum force applied to the needle at any point during the needle penetration test for the six different scaffold designs. The 45°/1layer sample demonstrated the lowest force of 2.43 N while the other samples demonstrated up to 46% greater forces (2.83 - 3.56 N). Typical suturing forces may be in the region of 2 - 8 N [45-47]. Plots for average needle force as a function of penetration depth are given in **Figure 9b**. The average force was at a maximum when the needle cut through polymer to exit the scaffold at depth 2-3 mm. **Figure 9c** shows three plots for average needle force versus displacement for 90°/3layer tests. Each plot is the average for all needle tests occupying a given starting penetration position shown in **Figure 2g**.

Figure 10a and **10b** show three scenarios that represent the three needle starting penetration positions indicated on **Figure 2g**:

- Position 1. The needle passed through a pore to enter the scaffold and cut through polymer to exit.
- Position 2. The needle cut polymer on entry but exited via a pore.
- Position 3: The needle cut through a series of polymer strands oriented perpendicular to the needle.

All plots in **Figure 9c** demonstrate peaks when the needle cut through polymer: at depths of 0.8 mm and 2.7 mm for positions 2 and 1, respectively, and every 0.6 mm for position 3. In addition to a cutting force peaks, the plots also show a friction force as the needles pass over polymer. This caused the peaks in the position 3 plot to increase in magnitude as the number of polymer strands in contact with the needle increased. Positions 1 and 3 demonstrated a greater peak force than position 2 because cutting occurred deeper into the scaffold when friction forces were greater.

Post-test analysis of the 2 and 3 *repeated layer* samples showed that position 1 occurred more frequently in the 45° *end angle* samples (74%) than in the 90° samples (52%), which could be due to the 45° *end angle* guiding needles into pores as shown schematically in **Figure 10c**. Since position 1 has a greater peak force than position 2, the 45° samples had a greater average peak force for 2 and 3 *repeated layers* compared to 90° samples (**Figure 9a**). The 45°/1layer scaffold had less fused polymer at the *side-wall* and therefore demonstrated the lowest cutting forces. In addition, it was infiltrated with the most cells for dynamic seeding and second-most for static seeding and demonstrated above average cell proliferation.

The results show that the 3D printed *side-wall* has a significant effect on the mechanics of a needle penetrating a porous scaffold. Although the forces are relatively small for our PCL samples, many bioresorbable polymers are much stiffer, in which case it is important to design scaffold structures with optimised suturing forces.

4. Conclusion

Our study quantified the effect of surfaces of 3D-printed scaffolds on mechanical properties, cell infiltration and proliferation and surgical suturing needle penetration forces. The control of *end angle* and *repeated layers* during 3D printing path design and manufacturing enabled a range of surface porosities from 2.5% to 20.1% and surface pore sizes from 0.01 - 0.26 mm² to be investigated. Variation of the 3D printed surface was found to affect compressive modulus by up to 36% and suturing needle penetration forces by almost 50%. In addition, increasing surface porosity enabled up to 55% more cells to be seeded within the scaffolds during dynamic seeding and up to 110% greater cell proliferation over 14 days. The results demonstrate that the external surface is an important factor for 3D printed scaffolds and that the presented method is able to control it.

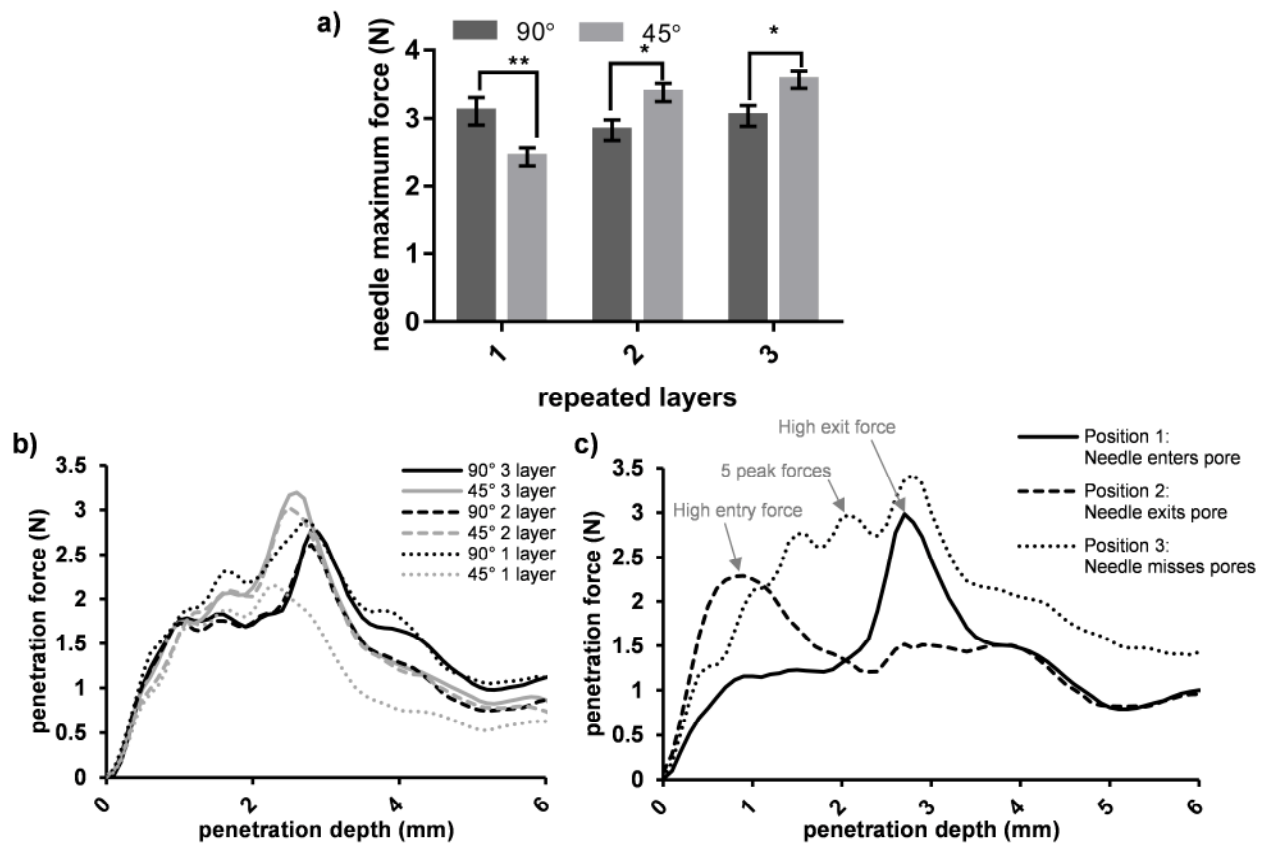


Figure 9. (a) Maximum needle penetration forces for the different scaffolds (average of 20 tests for each scaffold). (b) Needle penetration force versus penetration distance for the different scaffolds (each plot averages 20 tests). (c) Needle penetration force versus penetration distance for three scenarios of needle penetration in the 90°/3layer sample as described in in **Figure 10** (plots for position 1, 2 and 3 are the average of 8, 4 and 3 tests, respectively). * $p < 0.05$ ** $p < 0.009$

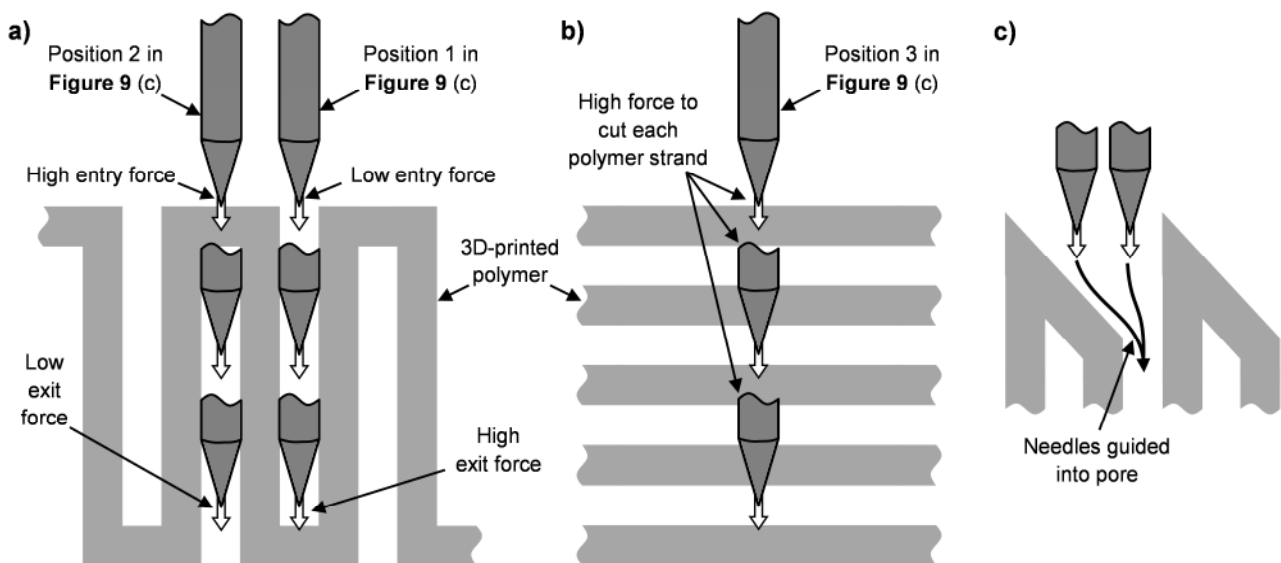


Figure 10. Schematic of the needle penetration positions considered in the **Figure 9** (c) plots. (a) Position 1: needle enters the scaffold through a pore and exits by penetrating polymer. Position 2: needle penetrates polymer on entry then exits through a pore. (b) Position 3: needle penetrates through multiple polymer strands. (c) The 45° end angle may guide needles into a pore.

Acknowledgments

The research leading to these results has received funding from the EPSRC [grant number EP/H028277/1] in the EPSRC Centre for Innovative Manufacturing in Regenerative Medicine. We thank CONACYT Mexico for sponsoring the studentship for Laura Ruiz-Cantu.

References

- [1] Murphy S V and Atala A 2014 3D bioprinting of tissues and organs *Nature biotechnology* **32** 773-85
- [2] Zopf D A, Flanagan C L, Wheeler M, Hollister S J and Green G E 2014 Treatment of severe porcine tracheomalacia with a 3-dimensionally printed, bioresorbable, external airway splint *JAMA otolaryngology-- head & neck surgery* **140** 66-71
- [3] Duan B, Kapetanovic E, Hockaday L A and Butcher J T 2014 Three-dimensional printed trileaflet valve conduits using biological hydrogels and human valve interstitial cells *Acta Biomaterialia* **10** 1836-46
- [4] Reiffel A J *et al* 2013 High-Fidelity Tissue Engineering of Patient-Specific Auricles for Reconstruction of Pediatric Microtia and Other Auricular Deformities *PLoS ONE* **8**
- [5] Lee C H, Cook J L, Mendelson A, Muioli E K, Yao H and Mao J J 2010 Regeneration of the articular surface of the rabbit synovial joint by cell homing: a proof of concept study *The Lancet* **376** 440-8
- [6] Lee C H, Rodeo S A, Fortier L A, Lu C, Eriskin C and Mao J J 2014 Protein-releasing polymeric scaffolds induce fibrochondrocytic differentiation of endogenous cells for knee meniscus regeneration in sheep *Science Translational Medicine* **6** 266ra171-266ra171
- [7] Morrison R J, Hollister S J, Niedner M F, Mahani M G, Park A H, Mehta D K, Ohye R G and Green G E 2015 Mitigation of tracheobronchomalacia with 3D-printed personalized medical devices in pediatric patients *Science Translational Medicine* **7**
- [8] Bose S, Vahabzadeh S and Bandyopadhyay A 2013 Bone tissue engineering using 3D printing *Materials Today* **16** 496-504
- [9] Probst F, Hutmacher D, Müller D, Machens H and Schantz J 2010 Rekonstruktion der Kalvaria durch ein präfabriziertes bioaktives Implantat [Calvarial reconstruction by customized bioactive implant] *Handchir Mikrochir plast Chir* **42** 369-73
- [10] Cohen A, Laviv A, Berman P, Nashef R and Abu-Tair J 2009 Mandibular reconstruction using stereolithographic 3-dimensional printing modeling technology *Oral Surgery, Oral Medicine, Oral Pathology, Oral Radiology, and Endodontology* **108** 661-6
- [11] Jetze V, Peters B, Burger T, Boomstra J, Dhert W, Melchels F and Malda J 2013 Biofabrication of multi-material anatomically shaped tissue constructs *Biofabrication* **5** 035007
- [12] Melchels F P, Domingos M A, Klein T J, Malda J, Bartolo P J and Hutmacher D W 2012 Additive manufacturing of tissues and organs *Progress in Polymer Science* **37** 1079-104

- [13] Domingos M, Dinucci D, Cometa S, Alderighi M, Bártolo P J and Chiellini F 2009 Polycaprolactone Scaffolds Fabricated via Bioextrusion for Tissue Engineering Applications *International journal of biomaterials* 2009
- [14] Masood S H 2007 Application of fused deposition modelling in controlled drug delivery devices *Assembly Automation* **27** 215-21
- [15] Leong K, Cheah C and Chua C 2003 Solid freeform fabrication of three-dimensional scaffolds for engineering replacement tissues and organs *Biomaterials* **24** 2363-78
- [16] Patrício T, Domingos M, Gloria A and Bártolo P 2013 Characterisation of PCL and PCL/PLA Scaffolds for Tissue Engineering *Procedia CIRP* **5** 110-4
- [17] Moroni L, de Wijn J R and van Blitterswijk C A 2006 3D fiber-deposited scaffolds for tissue engineering: influence of pores geometry and architecture on dynamic mechanical properties *Biomaterials* **27** 974-85
- [18] Murphy C M, Haugh M G and O'Brien F J 2010 The effect of mean pore size on cell attachment, proliferation and migration in collagen-glycosaminoglycan scaffolds for bone tissue engineering *Biomaterials* **31** 461-6
- [19] Wang M O *et al* 2015 Evaluating 3D - Printed Biomaterials as Scaffolds for Vascularized Bone Tissue Engineering *Advanced Materials* **27** 138-44
- [20] Rouwkema J, Rivron N C and van Blitterswijk C A 2008 Vascularization in tissue engineering *Trends in biotechnology* **26** 434-41
- [21] Sicchieri L G, Crippa G E, de Oliveira P T, Beloti M M and Rosa A L 2012 Pore size regulates cell and tissue interactions with PLGA–CaP scaffolds used for bone engineering *Journal of Tissue Engineering and Regenerative Medicine* **6** 155-62
- [22] Frick T B, Marucci D D, Cartmill J A, Martin C J and Walsh W R 2001 Resistance forces acting on suture needles *Journal of Biomechanics* **34** 1335-40
- [23] van Gerwen D J, Dankelman J and van den Dobbelsteen J J 2012 Needle–tissue interaction forces – A survey of experimental data *Medical Engineering & Physics* **34** 665-80
- [24] Jiang S, Li P, Yu Y, Liu J and Yang Z 2014 Experimental study of needle–tissue interaction forces: Effect of needle geometries, insertion methods and tissue characteristics *Journal of Biomechanics* **47** 3344-53
- [25] Hunziker E B and Stähli A 2008 Surgical suturing of articular cartilage induces osteoarthritis-like changes *Osteoarthritis and Cartilage* **16** 1067-73
- [26] Woodruff M A and Hutmacher D W 2010 The return of a forgotten polymer—Polycaprolactone in the 21st century *Progress in Polymer Science* **35** 1217-56
- [27] Martinez-Diaz S *et al* 2010 In Vivo Evaluation of 3-Dimensional Polycaprolactone Scaffolds for Cartilage Repair in Rabbits *The American Journal of Sports Medicine* **38** 509-19
- [28] Khan A J and Cook B C 2000 Wound healing and scar formation, *in* Harahap M. Surgical techniques for cutaneous scar revision. New York: Marcel Dekker

- [29] Buizer A T, Veldhuizen A G, Bulstra S K and Kuijer R 2013 Static versus vacuum cell seeding on high and low porosity ceramic scaffolds *Journal of biomaterials applications* **29** 3-13
- [30] Horn C E, Honrado C P and Khosh M M 2004 CLosure of conchal cartilage harvest sites via absorbable quilting suture *Archives of Facial Plastic Surgery* **6** 202-3
- [31] Toriumi D M and Asher S A 2015 Lateral Crural Repositioning for Treatment of Cephalic Malposition *Facial Plastic Surgery Clinics of North America* **23** 55-71
- [32] Travelute C R and Cartee T V 2013 Straight suture needle for full-thickness skin graft fixation on the ear *Journal of drugs in dermatology: JDD* **12** 104-5
- [33] Gassner H G 2010 Structural grafts and suture techniques in functional and aesthetic rhinoplasty *GMS Current Topics in Otorhinolaryngology, Head and Neck Surgery* **9**
- [34] Eshraghi S and Das S 2010 Mechanical and microstructural properties of polycaprolactone scaffolds with one-dimensional, two-dimensional, and three-dimensional orthogonally oriented porous architectures produced by selective laser sintering *Acta Biomaterialia* **6** 2467-76
- [35] Chin Ang K, Fai Leong K, Kai Chua C and Chandrasekaran M 2006 Investigation of the mechanical properties and porosity relationships in fused deposition modelling-fabricated porous structures *Rapid Prototyping Journal* **12** 100-5
- [36] Richmon J D, Sage A, Wong W V, Chen A C, Sah R L and Watson D 2006 Compressive biomechanical properties of human nasal septal cartilage *Am J Rhinol* **20** 496-501
- [37] Shepherd D E and Seedhom B B 1999 The 'instantaneous' compressive modulus of human articular cartilage in joints of the lower limb *Rheumatology* **38** 124-32
- [38] Black J and Hastings G 1998 Handbook of biomaterial properties. London: Chapman & Hall 40-47
- [39] Zein I, Hutmacher D W, Tan K C and Teoh S H 2002 Fused deposition modeling of novel scaffold architectures for tissue engineering applications *Biomaterials* **23** 1169-85
- [40] Bartnikowski M, Klein T J, Melchels F P and Woodruff M A 2014 Effects of scaffold architecture on mechanical characteristics and osteoblast response to static and perfusion bioreactor cultures *Biotechnology and bioengineering* **111** 1440-51
- [41] Al-Munajjed A A, Hien M, Kujat R, Gleeson J P and Hammer J 2008 Influence of pore size on tensile strength, permeability and porosity of hyaluronan-collagen scaffolds *Journal of Materials Science: Materials in Medicine* **19** 2859-64
- [42] Hutmacher D W, Schantz T, Zein I, Ng K W, Teoh S H and Tan K C 2001 Mechanical properties and cell cultural response of polycaprolactone scaffolds designed and fabricated via fused deposition modeling *Journal of biomedical materials research* **55** 203-16
- [43] Hutmacher D W 2000 Scaffolds in tissue engineering bone and cartilage *Biomaterials* **21** 2529-43
- [44] Mitsak A G, Kemppainen J M, Harris M T and Hollister S J 2011 Effect of Polycaprolactone Scaffold Permeability on Bone Regeneration In Vivo *Tissue Engineering Part A* **17** 1831-9

- [45] Dubrowski A, Larmer J C, Leming J K, Brydges R, Carnahan H and Park J 2006 Quantification of process measures in laparoscopic suturing *Surgical Endoscopy And Other Interventional Techniques* **20** 1862-6
- [46] Holton L 2001 Force models for needle insertion created from measured needle puncture data, *in* Westwood J. *Medicine Meets Virtual Reality 2001: Outer Space, Inner Space, Virtual Space*. Amsterdam: IOS Press
- [47] Jackson R C and Çavuşoğlu M C 2012 Modeling of needle-tissue interaction forces during surgical suturing *ICRA* 4675-80